POLITECNICO DI TORINO
Repository ISTITUZIONALE

A multiscale hybrid approach for vasculogenesis and related potential blocking therapies

(Article begins on next page)

18 April 2024

A Multiscale Hybrid Approach For Vasculogenesis and Related Potential Blocking Therapies

Marco Scianna^{A,B}, Luca Munaron^{C} and Luigi Preziosi^{A,1}

^{A} Department of Mathematics, Politecnico di Torino, Corso Duca degli Abruzzi 24, 10129 Torino, Italy

^{B} Institute for Cancer Research and Treatment, Strada Provinciale 142, 10060 Candiolo, Italy

^{C} Department of Animal and Human Biology, Nanostructured Interfaces and Surfaces Centre of Excellence (NIS), Center for Complex Systems in Molecular Biology and Medicine (SysBioM), Universita' degli Studi di Torino, via Accademia Albertina 13, 10123, Torino, Italy

Abstract

Solid tumors must recruit and form new blood vessels for maintenance, growth and detachments of metastases. Discovering drugs that block malignant angiogenesis is thus an important approach in cancer treatment and has given rise to multiple *in vitro* and *in silico* models. The present hybrid individual cell-based model incorporates some underlying biochemical events relating more closely the classical Cellular Potts Model (CPM) parameters to subcellular mechanisms and to the activation of specific signaling pathways. The model spans the three fundamental biological levels: at the extracellular level a continuous model describes secretion, diffusion, uptake and decay of the autocrine VEGF; at the cellular level, an extended lattice CPM, based on a system energy reduction, reproduces cell dynamics such as migration, adhesion and chemotaxis; at the subcellular level, a set of reaction-diffusion equations describes a simplified VEGF-induced calcium-dependent intracellular pathway. The results agree with the known interplay between calcium signals and VEGF dynamics and with their role in malignant vasculogenesis. Moreover, the analysis of the link between the microscopic subcellular dynamics and the macroscopic cell behaviors confirms the efficiency of some pharmacological interventions that are currently in use and, more interestingly, proposes some new therapeutic approaches, that are counter intuitive but potentially effective.

Keywords: cellular potts model · vascular endothelial growth factor · tubulogenesis · calcium

1 Introduction

Blood vessel formation and development is a multiscale process, driven by the activation of endothelial cells (ECs) and occurring both in the embryo and in the adult (for a review, see [13]). In the adult, vascular progression plays a key role under several physiological conditions, such as in ovary and uterus during the menstrual cycle, in mammary glands during lactation and in granulation tissue after wound healing. It is a complex and highly regulated phenomenon, controlled by coordinated molecular and cellular events operating at different levels. When this equilibrium is disrupted vascularization becomes pathological, as in the cases of chronic inflammatory diseases, vasculopathies, degenerative disorders, tissue injury occurring in ischemia, and cancer progression [15]. In particular, tumor-derived vessels, which differ from their "normal" counterpart in morphology (with irregular diameters, high tortuosity, random branching and absence of a hierarchical arrangement), permeability and blood flow [4, 12, 32], provide the nutrition and oxygen needed by malignant cells to grow, and give them an access into the circulation, eventually causing metastases

---

^{1}Corresponding Author. E-Mail: luigi.preziosi@polito.it

[13, 15]. The switch to the vascular phenotype is thus a pivotal transition in cancer development, leading to a fast progression and to a potentially fatal stage of tumors beyond which they become extremely difficult to treat. Existing therapies are in fact rarely effective and, consequently, the survival rates decrease [14, 74]. The discovery of efficient anti-angiogenic therapies represents therefore a fundamental issue in biomedical research [16] and has given rise to multiple experimental models (see reviews [3, 13, 53]), whose aim is to understand the key mechanisms involved in malignant vascularization and to identify interventions potentially able to disrupt them.
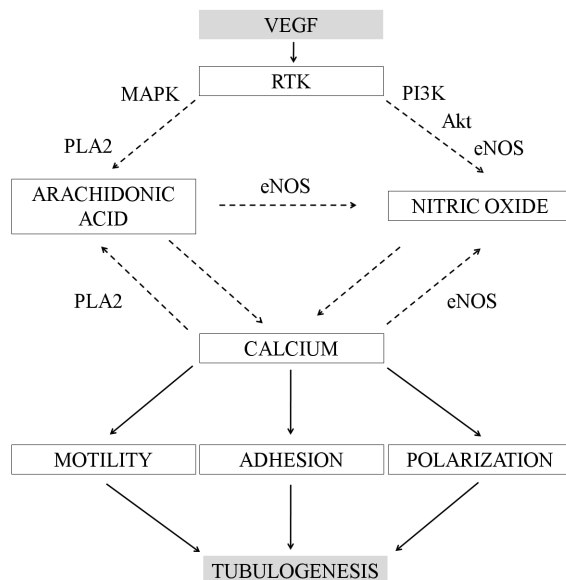

Figure 1: Simplified schematic representation of VEGF signaling cascades in the control of tumor-derived endothelial cell tubulogenesis. VEGF tyrosine kinase receptors activate a series of intracellular events inducing the recruitment of phospholipases A2 (PLA2) and eNOS and the subsequent release of arachidonic acid (AA) and nitric oxide (NO) respectively. Both intracellular messengers are able to activate plasma-membrane calcium channels. Increases in cytosolic calcium levels trigger motility, adhesion and cytoskeletal reorganization of TECs, crucial events for the capillary-like network formation. The dashed arrows stand for indirect pathways not completely included in the model.

Among others, classic *tubulogenic* assays analyze the ability of tumor-derived endothelial cells (TECs), cultured in Matrigel (a commercial product mimicking the extracellular matrix), to autonomously organize in a bidimensional network, which resembles a primitive *in vivo* capillary-like plexus [20]. This process, also called *in vitro vasculogenesis*, is largely mediated by the activity of diffusible chemical morphogens (such as VEGF isoforms [16]). They in fact initiate a series of calcium-dependent downstream pathways, which involve a number of intracellular messengers (such as nitric oxide (NO) and arachidonic acid (AA) [10, 21, 23, 34, 46, 48]) and regulate fundamental biophysical properties of TECs, such as motility, adhesion and elongation [7, 47, 49, 51, 52, 63], see Fig. 1. Indeed, the complexity of these multilevel mechanisms presents a number components that could be interfered in multiple ways to inhibit malignant vascular progression. This large combinatorial space of possible therapies is obviously unfeasible to search using only laboratory-based biological methods, but can be efficiently analyzed with computational simulations realistically reproducing the experimental system. With this aim, we propose a multilevel and hybrid search-based model replicating the *in vitro* TEC *tubulogenesis*. As shown in Fig. 2, it integrates:

- at the cellular level, an extended Cellular Potts Model (CPM), a lattice-based Monte Carlo technique which follows an energy minimization philosophy [25, 26, 29, 39], is the core of the simulation system and describes the phenomenology of TEC population, capturing the mechanisms of cell migration, polarization and adhesion. With respect to previous applications of the CPM, the model presented here is characterized by an innovative and realistic compartmentalized cell approach;

- at the molecular level a continuous model describes the extracellular VEGF profile, dealing with its production, diffusion and degradation, while a set of reaction-diffusion equations reproduces simplified intracellular VEGF-induced cascades, which regulate cytosolic calcium entry and homeostasis.

The interface of these multiple submodels is another novel feature of this work. In fact, differently from previous similar individual cell-based approaches [6, 41, 42, 43], cells properties, behaviors and mutual interactions are in this case regulated by the VEGF-induced calcium-dependent molecular dynamics, via reasonable simplified intracellular cascades, and the whole capillary network thus emerges as a consequence of realistic and relevant biochemical and biomechanical mechanisms.
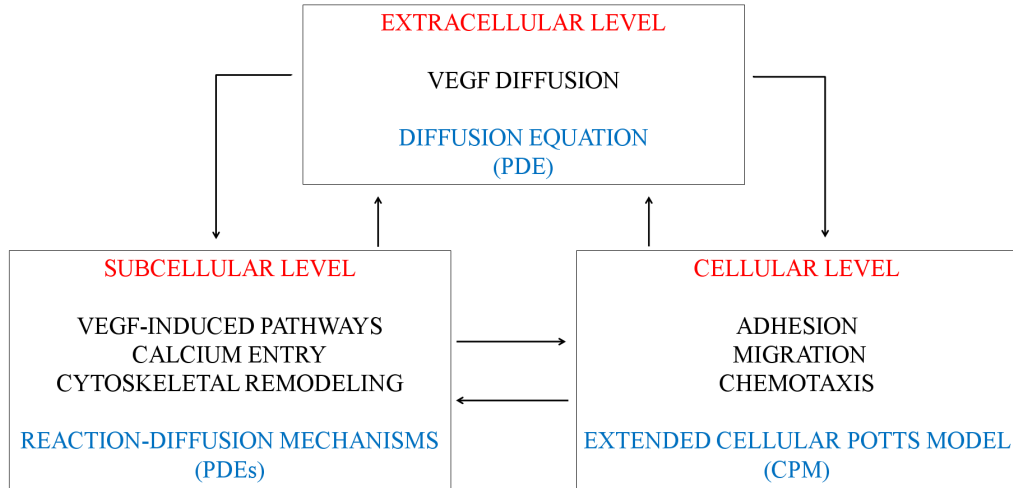

Figure 2: Hierarchy of scales and environments, corresponding biological mechanisms and modeling approaches. Information flows from microscopic biochemical processes to macroscopic phenomenology and *vice versa*.

The rest of this paper is organized as follows. We first clarify in Section 2 the assumptions on which our cell-based approach is based. We then show, in Section 3, the model capability to realistically reproduce selected features of *tubulogenic* assays. Then, after confirming the efficiency of some currently available therapies, we turn to suggest novel and experimentally testable strategies, which have the potential to disrupt TEC capillary formation. Finally, in Section 4, we discuss our results and propose some interesting extensions and improvements of the work.

2 Mathematical Model

Our multilevel model is based on the following set of assumptions, see again Fig. 1 for a diagrammatic representation:

- the TECs release VEGF in the extracellular medium, where it diffuses and degrades at constant rate [6, 24, 41, 43, 68, 76];

- VEGF acts as a chemoattractant for the cells, which move in the direction of increasing chemical concentrations: in particular, empirical data suggest that, because of the high viscosity of the experimental Matrigel, their motion is overdamped and the force required is proportional to the velocity, and thus to the chemical gradient [2, 42, 76];

- during migration TECs remodel their cytoskeleton and polarize, differentiating in a leading and a trailing surface. The resulting elongated morphology causes TEC to have an anisotropic migration (e.g., persistence) in the direction of their longer axis [2, 31, 59]. Such a shape-dependent motility is essential for cell alignment in vascular chords, as demonstrated in [31, 42];

- VEGF mediates the overall process also by binding specific cell surface tyrosine kinase receptors and by initiating a sequence of intracellular cascades, which result in the indirect production of second messengers arachidonic acid (AA) and nitric oxide (NO) in the sub plasmamembrane regions [10, 23, 34, 46, 47, 75]. These biochemical events are triggered, respectively, by enzymes PLA2 and eNOS, whose activity is not explicitly included in our model, since it does not influence its final outcome;

- NO and AA diffuse and degrade in a finite time, producing eicosanoids [33] and peroxynitrites [57], respectively;

- within cell cytosol NO production is triggered also by AA itself [21, 46, 48];

- NO and AA open the relative and independent calcium channels in the cells' plasmamembrane, leading to extracellular calcium entry [20, 21, 46, 47, 75, 78].

- calcium ions, which are reversibly buffered by proteins including calmodulin and others and mitochondria (with a strong influence in the effective diffusion and a decrease in the overall level [1, 5, 7, 8, 11, 35]), mediates cell biophysical properties such as motility, adhesion strength, cytoskeletal elasticity, and chemotactic response [7, 47, 49, 51, 52, 63]. Finally, Ca^{2+}, which also enhances the rates of AA and NO biosynthesis within cell cytosolic region with a positive feedback mechanism [47], can be subsequently extruded back from cells by plasmamembrane calcium ATPase and Ca^{2+}-Na^+ exchangers [28, 30, 77].

It is useful to stress that TECs phenomenology is mesoscopically described with the discrete Cellular Potts Model, while both the extracellular VEGF dynamics and the intracellular VEGF-induced calcium-dependent cascades are approached with standard continuous methods. These different submodels are then interfaced and integrated in a hybrid environment, and directly impact each others, with a constant interplay and flux of information between the different levels, as we explicitly clarify in the remainder of this section.

2.1 Cell-Level Model

The natural level defined in *in vitro* capillary formation is the cell. Accordingly, the core of our simulation framework is an extended Cellular Potts Model, which naturally handles individual cell behaviors and interactions. The CPM is a discrete lattice Monte Carlo generalization of the Ising's model, based on an energy minimization principle. All CPM applications represents the simulated system on a numerical grid (in this work, since we wish to compare our simulations to experimental cultures, where the vascular networks are essentially monolayers, we use a bidimensional domain [41, 42, 43, 68]), where each site $\mathbf{x}$ is labeled with an integer index, $\eta(\mathbf{x})$. Collection of lattice sites with the same index represent discrete objects, which can also have an additional attribute, a type $\tau(\eta)$. The borders between sites with different spins define objects' membranes. In classic CPMs the cells are typically treated as undifferentiated objects, which can rearrange to produce cell motion and shape changes. We here introduce an innovative and realistic compartmentalized cell extension of the CPM (see Discussion for a more detailed comment): the lattice subdomains do not represent whole cells, but subcellular compartments which, in turn, form the considered individual cells. In particular, within the same cell, σ, we differentiate between the nucleus (a central cluster of type $\tau = N$, whose location and geometry is estimated from experimental images) and the surrounding cytosolic region of $\tau = C$, as shown in Fig. 3. The plasma and the nuclear membranes are defined as the borders between the cytosolic compartment and, respectively, the medium and the nuclear region. Obviously, this is a more biologically accurate representation of cells, whose dimensions are given in Table I and reflect the most usual morphologies observed in classical cultures [20, 54, 75]. The extracellular environment, e.g. the experimental-like Matrigel, is modeled as a special generalized cell $\sigma = 0$ of type $\tau = M$. It is assumed to be homogenously distributed throughout the simulation domain, forming no large-scale structures and thus without volume or surface attributes as done in [41, 42, 43]. The extracellular substrate is also static and passive: cells can only change it by occupying sites that, once abandoned, return to a matrix state.

The TECs gradually and iteratively rearrange to reduce a pattern effective energy, given by an hamiltonian H. The functional H contains a variable number of terms, consisting in cell attributes (e.g. volume, surface), true energies (e.g. cell-cell adhesions), and terms mimicking energies (e.g., response to external chemical stimuli), and its local gradient is the "force" acting in any point of the simulation domain. The energy minimization core algorithm is a modified

	(1,C)	(1,C)	(1,C)					
(1,C)	(1,C)	(1,N)	(1,C)	(1,C)				
(1,C)	(1,N)	(1,N)	(1,N)	(1,C)				
(1,C)	(1,C)	(1,N)	(1,C)	(1,C)		(2,C)	(2,C)	(2,C)
	(1,C)	(1,C)	(1,C)		(2,C)	(2,C)	(2,N)	(2,C)	(2,C)
					(2,C)	(2,N)	(2,N)	(2,N)	(2,C)
E	C	M	(0 , M)	(2,C)	(2,C)	(2,N)	(2,C)	(2,C)
						(2,C)	(2,C)	(2,C)

Figure 3: The typical CPM grid and representation of compartmentalized cells and ECM. Each lattice site $\mathbf{x}$ is uniquely characterized by the couple $(\sigma(\mathbf{x}), \eta(\mathbf{x}))$, denoting, respectively, the cell and the subcompartment it belongs to. In the figure there are two different cells and their virtual Matrigel, lattice locations labeled with (0,M). The bold lines denote cell boundaries.

Metropolis method for Monte Carlo dynamics [29, 45]. It is able to implement the natural exploratory behavior of biological individuals, via thermal membrane fluctuations and biased extensions and retractions of their membranes. Procedurally, a lattice site, $\mathbf{x}_{source}$, is selected at random and assigns its state (σ, η) to one of its unlike neighbors, $\mathbf{x}_{target}$, which has also been randomly selected. The hamiltonian of the system is computed before and after the proposed update: if H is reduced as the result of the copy, the change is accepted, else the Boltzmann probability function

$$P(\Delta H) = \begin{cases} e^{-\Delta H/T} & \Delta H > 0 \, ; \\ 1 & \Delta H \leq 0 \, , \end{cases} \tag{2.1}$$

is used, where ΔH is the net difference in the system energy and T is an effective Boltzmann temperature. A total of n proposed updates, where n is the number of sites of the lattice, constitutes a Monte Carlo Step (MCS), which is the basic iteration and the unit of time used in the model. Classic CPMs use a temperature T constant for the whole system, giving the idea of a generic and homogeneous "culture motility" [41, 42, 43, 65]. We instead define T as a sort of agitation rate relative to the moving compartment: $T = T(\eta(\mathbf{x}_{source}))$. Specifically, for each TEC σ and for $\tau(\eta(\mathbf{x}_{source})) = N$, $T(\eta(\mathbf{x}_{source})) = T_N$ is a constant low value mimicking the passive motion of the nucleus, which is dragged by the surrounding cytosolic region. For $\tau(\eta(\mathbf{x}_{source})) = C$, $T(\eta(\mathbf{x}_{source}))$ is instead a measure of the intrinsic motility of σ, the cell to which $\mathbf{x}_{source}$ belongs. It in fact qualitatively reproduces the frequency of the continuous, random extensions and retractions of cytosolic cells' pseudopods, which is mediated by the intracellular calcium concentration in a dose-dependent manner, as provided by wound healing experiments [22]:

$$T = T(\eta(\mathbf{x}_{source})) = T_0 \left[\frac{1 + \widetilde{Ca}(\sigma)}{1 + h\widetilde{Ca}(\sigma)} \right], \tag{2.2}$$

where σ is, as seen, the TEC to which cytosolic compartment $\eta(\mathbf{x}_{source})$ belongs to. Moreover, here and in the following, $\widetilde{Ca}(\sigma) = [Ca(\sigma)/Ca_0] - 1$ is a positive value, since $Ca(\sigma) = \sum_{\mathbf{x} \in \sigma} Ca(\mathbf{x})$ corresponds to the actual total calcium concentration of σ, that must be larger than Ca_0, the basal level of the ion in resting TECs (below which the cells die). The value of Ca_0 can be experimentally estimated (see Table I) and used to evaluate, by comparison with biological cultures, the basal properties of the simulated cells, such as basal motility T_0. The generalization to more cell populations each with a different calcium dependent motility is straightforward.

The hamiltonian of the TEC culture, whose minimization, as seen, drives the patterning is:

$$H = H_{shape} + H_{adhesion} + H_{chemical} + H_{persitence}. \tag{2.3}$$

5

H_{shape} takes into account of cell-shape remodeling, which can be active, due to cytoskeletal stresses, or passive, due to mechanical strains, differential adhesion or as a result of the migration of other cells. Such deformations cause energy changes, which are written in the following elastic-like form:

$$H_{shape} = H_{area} + H_{perimeter} = \sum_{\sigma,\eta} \left[\mu_a(\sigma,\eta)(a_{\sigma,\eta} - A_{\tau(\eta)})^2 + \mu_p(\sigma,\eta)(p_{\sigma,\eta} - P_{\tau(\eta)})^2 \right], \qquad (2.4)$$

where $a_{\sigma,\eta}$ and $p_{\sigma,\eta}$ are, respectively, the actual surface and perimeter of compartment η of cell σ, while $A_{\tau(\eta)}$ and $P_{\tau(\eta)}$ are their target measures (the dimensions of the nucleus and the cytosol region which a typical TEC would have in absence of external forces and in the presence of adequate nutrients, see Table I). μ_a and μ_p are penalty coefficients controlling, respectively, the growth and the elasticity of the subcellular compartments (e.g., deviations of $a_{\sigma,\eta}$ and $p_{\sigma,\eta}$ from $A_{\tau(\eta)}$ and $P_{\tau(\eta)}$ increase the functional H). In accordance with the observation that the cells do not grow or divide during tubule formation [41, 42] and that their nuclei maintain the initial circular structure, for any σ we set high constant values of $\mu_a(\sigma,\eta)$, $\eta : \tau(\eta) = N, C$, and of $\mu_p(\sigma,\eta)$, for $\eta : \tau(\eta) = N$, see also Table I. For each TEC σ, $\mu_p(\sigma,\eta)$, where $\tau(\eta) = C$, is instead a measure of the ease with which it changes its shape. Since experimental data suggest that increases in cytosolic calcium facilitate cytoskeletal reorganization, almost in a dose-dependent manner, we set:

$$\mu_p(\sigma,\eta) = \mu_{p,0} \, \exp\left(-k\widetilde{Ca}(\sigma)\right), \qquad (2.5)$$

where $\mu_{p,0}$ is the intrinsic cells' resistance to compression at the same basal calcium concentration Ca_0 and $\widetilde{Ca}(\sigma)$ is as in Eq. (2.2). In particular, we use an exponential function because for high $\widetilde{Ca}(\sigma)$, $\mu_p(\sigma,\eta) \to 0$: this mimics the biologically provided fact that very high calcium levels promote continuous and dramatic actin-myosin interactions, resulting in quick changes in cell organization and shape in response to external stimuli (such as chemotaxis).

$H_{adhesion}$ phenomenologically implements the general extension of the Steinberg's differential adhesion hypothesis (DAH) [29, 72, 73]. Specifically, we introduce two hierarchies of contact energies, external and internal: the idea is to differentiate between the real cell-cell adhesion and the generalized contact energy between nuclei and cytosols within the same cells:

$$H_{adhesion} = H_{adhesion}^{ext} + H_{adhesion}^{int} =$$

$$= \sum_{\mathbf{x},\mathbf{x}'} \left[J_{C,C}^{ext}(\mathbf{x},\mathbf{x}')(1 - \delta_{\sigma(\mathbf{x}),\sigma(\mathbf{x}')}) + J_{C,N}^{int}(\mathbf{x},\mathbf{x}')(\delta_{\sigma(\mathbf{x}),\sigma(\mathbf{x}')})(1 - \delta_{\sigma(\mathbf{x}),\sigma(\mathbf{x}')}) \right], \qquad (2.6)$$

where $\mathbf{x}, \mathbf{x}'$ represent two neighboring lattice sites, $\delta_{x,y} = \{1, x = y; 0, x \neq y\}$ is the Kronecher delta, and the Js are binding energies per unit of area. Since, obviously, cells can not break in small fragments, we fix a high negative bond energy $J_{C,N}^{int}$ for each interface nucleus-cytosol. $J_{C,C}^{ext}(\mathbf{x},\mathbf{x}')$, where $\sigma(\mathbf{x}) \neq \sigma(\mathbf{x}')$, models instead the probability of formation of local intercellular VE-cadherin-VE-cadherin complexes between cells $\sigma(\mathbf{x})$ and $\sigma(\mathbf{x}')$. In particular, it is the joint probability that the calcium ions in each of the two cells enhances the local cadherins' avidity (in a dose dependent manner), biologically either with quantitative changes in their expression or with the activation of the already exposed molecules. The resulting function is then assumed to be:

$$J_{C,C}^{ext}(\mathbf{x},\mathbf{x}') = J_0 \, \exp\left(-j\widetilde{Ca}(\mathbf{x})\widetilde{Ca}(\mathbf{x}')\right), \qquad (2.7)$$

where $\widetilde{Ca}(\mathbf{x}) = [Ca(\mathbf{x})/(Ca_0/(a_{\sigma(\mathbf{x})}))] - 1$ is the local (e.g., per lattice site) mean of $\widetilde{Ca}(\sigma)$. J_0 represents the typical adhesive force of resting TECs, estimated by qualitative observations of experimental cultures. Also in this case we use an exponential function because high calcium levels result in $J_{C,C}^{ext}(\mathbf{x},\mathbf{x}') \to 0$, the computational counterpart of highly adhesive cells. The dramatic VEGF-induced calcium accumulation in the sub-plasmamembrane regions generates in fact clusters of VE-cadherins along the cell spreading front and in lamellipodia protrusions, which play a crucial role in the formation and stabilization of the nascent capillary network. We do not include the case of the contact between nuclei of different cells because the model will be such that they never touch, as well as we do not

consider an adhesion energy between the cells and the virtual Matrigel (i.e., $J_{C,M}^{ext} = 0$), since in our approach the extracellular medium is modeled only as a rigid and passive substratum.

The TEC overdamped chemotactic migration is implemented by including a linear term in the energy function [64]:

$$\Delta H_{chemotaxis} = \mu_{ch}(\sigma(\mathbf{x}_{source})) \left[Q(\mathbf{x}_{target}) - Q(\mathbf{x}_{source}) \right], \tag{2.8}$$

where $\mathbf{x}_{source}$ and $\mathbf{x}_{target}$ are, respectively, the source and the final lattice sites randomly selected during a trial update in a MCS: in particular $\mathbf{x}_{source}$ is a cytosolic site of cell σ and $\mathbf{x}_{target}$ is one of its medium neighbors (i.e., $\mathbf{x}_{source}$ is a cell membrane site of σ). The parameter μ_{ch} is the strength of the chemotactic response of cell σ:

$$\mu_{ch}(\sigma(\mathbf{x}_{source})) = \mu_{ch,0}\widetilde{Ca}(\sigma(\mathbf{x}_{source})), \tag{2.9}$$

where $\mu_{ch,0}$ is a basal chemical sensitivity. $\mu_{ch}(\sigma(\mathbf{x}_{source})) \geq 0$ because $\widetilde{Ca}(\sigma(\mathbf{x}_{source})) \geq 0$ as recalled after Eq. (2.2). This relation enforces the direct influence of the current calcium level in the avidity of VEGF surface receptors, whose activity mediates the cell chemotactic force. In particular, (2.9) is a strong improvement of this work w.r.t. similar models, where all simulated cells are assumed to experience the same chemical response, see [41, 42, 43]. Q is the measure of the local extracellular VEGF concentration V stimulating cell pseudopod extension:

$$Q(\mathbf{x}, V) = \sum_{\mathbf{x}'} V(\mathbf{x}'), \tag{2.10}$$

where $\mathbf{x} \in \{\mathbf{x}_{source}, \mathbf{x}_{target}\}$ and $\mathbf{x}'$ are all the matrix first-nearest neighbors of $\mathbf{x}$. However, the cell chemotactic response is also mediated by the homophilic transmembrane VE-cadherins which, as long as adhesion functions, have an important signaling role. They in fact act as local inhibitors of VEGF-induced pseudopodal extensions at cell-cell boundaries: consequently, only the interfaces between the cells and the medium respond to the chemical stimulus. This process, called *contact inhibition of chemotaxis*, has been widely demonstrated to possibly contribute to ECs' self organization into capillary networks and is modeled by imposing $\mu_{ch} = 0$ at cell-cell interfaces [43].

Normal motion in CPMs is Aristotelian: velocity is proportional to the applied force with no inertia, and the cells typically undergo a random walk with relatively short persistence lengths. While this dynamics is appropriate in several biological contexts, vascular cells are characterized by a persistent migration in the direction of their longer axis. To model such a cell-shape-dependent movement, a number of CPM extensions have preassigned target directions or target velocity components to each individual [39]. We instead derive cells' inertial motion from their instantaneous velocity, as a running mean over their past movements (as done also in [25, 65]):

$$H_{persistence} = \sum_{\sigma} \mu_{pers}(\sigma)||\mathbf{v}(\sigma, t) - \mathbf{v}(\sigma, t - \Delta t)||^2, \tag{2.11}$$

where

$$\mathbf{v}(\sigma, t) = \frac{\mathbf{cm}(\sigma, t) - \mathbf{cm}(\sigma, t - \Delta t)}{\Delta t} \tag{2.12}$$

is the instantaneous velocity of the center of mass of cell σ ($\mathbf{cm}(\sigma) = a^{-1}(\sigma) \sum_{\mathbf{x}:\sigma(\mathbf{x})=\sigma} \mathbf{x}$) and Δt is equal to one MCS. The function for the non-dimensional penalty coefficient μ_{pers} controlling the persistence time is:

$$\mu_{pers} = \mu_{pers,0} \left[\frac{L(\sigma)}{L_0} - 1 \right], \tag{2.13}$$

where $L(\sigma)$ is the current length of cell σ along its longer axis (derived from the inertia tensor approximating the virtual cells with ellipses) and L_0 its initial value (the initial cell diameter, see Table I). Obviously $L(\sigma) \geq L_0$, since we assume that the cells deform but do not grow during patterning. Equation (2.13) describes the fact that, after analogous chemical stimulations, elongated vascular cells have seen to have a longer persistent movement than round cells [31]. This is due to the increasing time needed by polarized actin filaments to reorient into a new direction. In particular, if $\mu_{pers} = 0$ cells undergo uncorrelated Brownian motion, while if μ_{pers} is very large the motion is almost ballistic. In this way, the cells' movements depend both on their past movement and on their internal state.

Parameter	Description	Model Value [Unit: 1 px ≈ 1 μM]	Reference
A_N	area of nuclear compartment	100 [μm^2]	[75]
P_N	perimeter of nuclear compartment	35 [μm]	[75]
A_C	area of cytosolic compartment	1150 [μm^2]	[75]
P_C	perimeter of cytosolic compartment	150 [μm]	[75]
T_0	basal TEC motility	4	
h	Michaelis-Menten coefficient for T	1/2	
$\mu_a(\sigma, N)$	area elasticity of nuclear compartment	-20	
$\mu_p(\sigma, N)$	nuclear membrane elasticity	-20	
$\mu_a(\sigma, C)$	volume elasticity of cytosolic compartment	-20	
$\mu_{p,0}$	plasma membrane elasticity	4	
k	Michaelis-Menten coefficient for μ_p	1	
$J^{int}(C, N)$	generalized nucleus-cytosol adhesion within the same cell	-20	
J_0	basal level of expression of VE-cadherin	4	
j	Michaelis-Menten coefficient for $J^{ext}((\,\cdot\,, C), (\,\cdot\,, C))$	1	
$\mu_{ch,0}$	basal chemotactic strength	4	
$\mu_{pers,0}$	basal inertia strength	4	

2.2 Microscopic Model

As seen, the evolution of the VEGF constitutes the extracellular environment the cells respond to, setting up a chemical gradient and activating downstream pathways. Mathematically, its spatial profile satisfies the following diffusion equation:

$$\frac{\partial V(\mathbf{x}, t)}{\partial t} = D_V \nabla^2 V(\mathbf{x}, t) - \lambda_V V(\mathbf{x}, t) - B(\mathbf{x}, t, V(\mathbf{x}, t)) + S(\mathbf{x}, t), \tag{2.14}$$

where $V(\mathbf{x}, t)$ denotes the local concentration of the peptide. The coefficient of diffusivity, $D_V > 0$, is assumed to be homogeneous throughout the simulated Matrigel and is derived from previous experimental determinations (even if the network formation holds over a large range of diffusion coefficients, although with different length scales, as shown [6, 42, 43]). The degradation rate of VEGF, λ_V, is also considered constant. $S(\mathbf{x}, t)$ describes the autocrine secretion of the growth factor from cells' membrane at a constant rate ϕ_V per unit of time. The VEGF binding and uptake by tumor-derived ECs is defined with $B(\mathbf{x}, t, V(\mathbf{x}, t))$ and is limited to a maximum rate of $\beta_V > 0$ over the external surface of cells:

$$B(\mathbf{x}, t, V(\mathbf{x}, t)) = \min\{\beta_V, vV(\mathbf{x}, t)\} \tag{2.15}$$

where $\mathbf{x}$ are all the extracellular neighbors of a cell site (i.e., $\tau(\eta(\mathbf{x})) = M$ and $\tau(\eta(\text{neighbor of } \mathbf{x})) = C$). This is realistic since the capacity of a cell to locally uptake the growth factor will saturate to a rate-limit, β_V, which is the amount of molecules that can be bound and internalized per unit of time. To compute β_V (whose value is given in Table II), we consider the density of VEGF receptors per unit area and the rate at which their complexes can be internalized and the receptor recycled, following [6].

As shown in Fig. 1, we include three distinct pathways for VEGF-induced calcium entry: two, shorter, and directly mediated by second messengers arachidonic acid (AA) and nitric oxide (NO) and another, longer, and mediated by NO recruitment by the fatty acid itself [46, 75]. The model of such intracellular events starts with equations regulating AA and NO dynamics, which account for their agonist-induced activation, diffusion with the cytosol, and gradual degradation. The multiple signal transduction proteins, that are known intermediates in AA and NO generation (such as, respectively, PLA2 and eNOS enzymes), are not directly included. The current levels of AA and NO at cell location $\mathbf{x}$ are defined, respectively, as $AA(\mathbf{x}, t)$ and $NO(\mathbf{x}, t)$, and are controlled by the following diffusion equations [54, 66]:

$$\frac{\partial AA(\mathbf{x}, t)}{\partial t} = D_{AA} \nabla^2 AA(\mathbf{x}, t) - \lambda_{AA} AA(\mathbf{x}, t) + v_{AA} R(\mathbf{x}, t, B) + c_{AA} Ca(\mathbf{x}, t) \tag{2.16}$$

$$\frac{\partial NO(\mathbf{x}, t)}{\partial t} = D_{NO} \nabla^2 NO(\mathbf{x}, t) - \lambda_{NO} NO(\mathbf{x}, t) + v_{NO} R(\mathbf{x}, t, B) + \frac{v_{Ca-AA} Ca(\mathbf{x}, t) AA(\mathbf{x}, t)}{(c_{NO} + Ca(\mathbf{x}, t))(a_{AA} + AA(\mathbf{x}, t))} \tag{2.17}$$

The coefficients of diffusivity, D_{AA}, $D_{NO} > 0$, are assumed to be homogeneous within the cells. The degradation of both the intracellular messengers is also considered constant, at rates λ_{AA}, $\lambda_{NO} > 0$. The third terms in Eqs. (2.16) and (2.17) describe the production rate at cells' membrane of AA and NO, triggered by the sequestrated VEGF molecules, as

$$R(\mathbf{x}, t) = \sum_{\mathbf{x'}} B(\mathbf{x'}, t), \tag{2.18}$$

where $B(\mathbf{x'}, t)$ is defined as in (2.15) and, in particular, the $\mathbf{x}$'s form the extracellular first-nearest neighborhood of the cytosolic site $\mathbf{x}$ (i.e., $\tau(\eta(\mathbf{x})) = C$ and $\tau(\eta(\mathbf{x'}-\text{neighbor})) = M$). The last term in Eq. (2.16) implements the calcium-dependent feedback mechanism in AA biosynthesis, while the analogous term in Eq. (2.17) accounts for the double regulation of NO production (both AA- and Ca-mediated), also depicted in Fig. 1. All these terms work within the entire cell domain.

For each cell σ, the intracellular level of calcium at site $\mathbf{x}$, defined as $Ca(\mathbf{x}, t)$, is generally determined by a balance of entry, efflux or extrusion from the cytosol, and buffering [19, 54, 66, 70], and it is controlled by the following reaction-diffusion equation:

$$\frac{\partial Ca(\mathbf{x}, t)}{\partial t} = \frac{K_{off}}{K_{off} + K_{on} b_T} \left[D_{Ca} \nabla^2 Ca(\mathbf{x}, t) + F_{AA}(\mathbf{x}, t) + F_{NO}(\mathbf{x}, t) - F_{out}(\mathbf{x}, t) \right]. \tag{2.19}$$

The coefficient of diffusion, $D_{Ca} > 0$, is assumed to be homogeneous troughout the cell (the diffusion of calcium across the nuclear envelope is taken to occur through non selective pores, whose permeability is proportional to the diffusion constant of the ion in the cytosol [18, 54, 66]). F_{out} describes the extrusion of the ion via plasmamembrane ATPases and Na-Ca exchangers (respectively PMCAs and NCXs), which are assumed to be restricted and uniformly distributed over the cells' surface. According to experimental evidence, the corresponding flux is a function of the calcium level, with a threshold behavior [19]. There is no flux below the critical concentration Ca_t, while above this level the flux grows linearly as a function of Ca itself:

$$F_{out}(\mathbf{x}, t) = F_{out}(Ca(\mathbf{x}, t)) = \begin{cases} k_{Ca}(Ca(\mathbf{x}, t) - Ca_t) & \text{if} \quad Ca(\mathbf{x}, t) \geq Ca_t \; ; \\ 0 & \text{else} \, , \end{cases} \tag{2.20}$$

where $\mathbf{x}$ is in the cell membrane, k_{Ca} is the constant rate of flux density.

F_{AA} and F_{NO} represent, respectively, the independent and either AA- or NO-activated calcium fluxes from the extracellular environment, which are passive and follow an electrochemical gradient. We assume a Michaelis-Menten form for both the distributions, representing the biophysical properties of fixed and uniformly distributed PM channels, whose permeabilities are proportional to the local concentration of intracellular messengers and exhibit threshold values experimentally found. In other words, at high concentrations of AA and NO the PM channels saturate, thus becoming insensitive to a further increase of AA and NO levels:

$$F_{AA}(\mathbf{x}, t) = F_{AA,max} \frac{(AA(\mathbf{x}, t)/AA_0)^m}{q_{AA} + (AA(\mathbf{x}, t)/AA_0)^m}, \tag{2.21}$$

$$F_{NO}(\mathbf{x}, t) = F_{NO,max} \frac{(NO(\mathbf{x}, t)/NO_0)^m}{q_{NO} + (NO(\mathbf{x}, t)/NO_0)^m}, \tag{2.22}$$

$\mathbf{x}$ belongs, as now usual, to the cells' membranes, and $AA(\mathbf{x}, t)$ and $NO(\mathbf{x}, t)$ are derived by Eqs. (2.16) and (2.17). We select a quadratic $m = 2$ sigmoidal activation and $q_{AA} = q_{NO} = 1$, with maximum fluxes saturating at concentrations $AA(\mathbf{x}, t) \gg AA_0$ and $NO(\mathbf{x}, t) \gg NO_0$ respectively. Although this is a very simple model, in the absence of more specific evidence [21, 53], it is acceptable for low agonist concentrations and it is experimentally validated [66, 71]. The scaling factor $\frac{K_{off}}{K_{off} + K_{on} b_T}$ models the activity of intracellular endogenous buffers: b_T is the total concentration of buffer sites (considered constant and experimentally estimated in different cell types), K_{on} is the rate of calcium uptake, and K_{off} the rate of its release. This approximation works in the case of immobile buffers, characterized by low affinity and fast kinetics [70, 71].

TABLE II

PARAMETERS GOVERNING THE MICROSCOPIC MODEL

PARAMETER	DESCRIPTION	MODEL VALUE	REFERENCE
D_V	diffusion constant of VEGF	$10\,[\mu\mathrm{m}^2\mathrm{s}^{-1}]$	[68]
λ_V	on-rate constant of VEGF degradation	$0.78\,[\mathrm{h}^{-1}]$	[68]
ϕ_V	on-rate constant of VEGF secretion	$0.78\,[\mathrm{h}^{-1}]$	[66, 68]
β_V	maximum amount of bound VEGF for unit of time	$0.06\,[\mathrm{pg/cell/h}]$	[6, 66]
v	coefficient of the amount of bound VEGF per unit of time	$1\,[h^{-1}]$	
D_{AA}	diffusion constant of AA	$10\,[\mu\mathrm{m}^2\mathrm{s}^{-1}]$	[54]
λ_{AA}	on-rate constant of AA degradation	$30\,[\mathrm{s}^{-1}]$	[54]
v_{AA}	on-rate constant of VEGF-dependent AA release	$30\,[\mathrm{s}^{-1}]$	[54]
c_{AA}	on-rate constant of Ca-dependent AA release	$5\,[\mathrm{s}^{-1}]$	
D_{NO}	diffusion constant of NO	$3300\,[\mu\mathrm{m}^2\mathrm{s}^{-1}]$	[54]
λ_{NO}	on-rate constant of NO degradation	$0.1\,[\mathrm{s}^{-1}]$	[54]
v_{NO}	on-rate constant of VEGF-dependent NO release	$30\,[\mathrm{s}^{-1}]$	
c_{NO}	dissociation constant between Ca and eNOS	$0.3\,[\mu\mathrm{M}]$	[54]
a_{AA}	dissociation constant between Ca and eNOS	$0.2\,[\mu\mathrm{M}]$	[54]
v_{Ca-AA}	maximal rate of NO release	$1.5\,[\mu\mathrm{Ms}^{-1}]$	[54]
D_{Ca}	diffusion constant of Ca	$220\,[\mu\mathrm{m}^2\mathrm{s}^{-1}]$	[19, 54]
k_{Ca}	average rate of calcium efflux density	$8\,[\mu\mathrm{ms}^{-1}]$	[19]
Ca_t	threshold concentration for calcium extrusion	$0.2\,[\mu\mathrm{M}]$	[19, 65]
C_0	basal TEC calcium level	$0.2\,[\mu\mathrm{M}]$	[19, 54]
$F_{AA,max}$	Michaelis-Menten constant of AA-induced calcium influx	$6\,[\mathrm{s}^{-1}]$	[66]
$F_{NO,max}$	Michaelis-Menten constant of NO-induced calcium influx	$4.5\,[\mathrm{s}^{-1}]$	[66]
AA_0	saturation level of AA	$5\,[\mu\mathrm{M}]$	
NO_0	saturation level of NO	$5\,[\mu\mathrm{M}]$	
K_{off}	dissociation constant between endogenous buffers and Ca_c	$2\,[\mu\mathrm{M}]$	[54]
K_{on}	on-rate constant of endogenous Ca_c buffering	$100\,[\mu\mathrm{M}^{-1}\mathrm{s}^{-1}]$	[54]
b_T	total endogenous buffer concentration	$450\,[\mu\mathrm{M}]$	[19]
$C_{ext,0}$	extracellular calcium level	$2000\,[\mu\mathrm{M}]$	[7, 54]

3   SIMULATIONS AND RESULTS

Our model framework is implemented with a modified version of the open-source Compucell3D[2] environment [27, 60], which is able to integrate all the proposed biological submodels, while maintaining their modularity. The grid for the numerical solution of the PDEs is in fact matched with the CPM lattice and, at every time step, each computational module is used as the initial condition for the others. Procedurally, after the discrete CPM has evolved through a MCS, the continuous equations are rederived, based on the new distribution of the cells, and solved using a finite element scheme, characterized by 10 diffusion time steps per MCS. In particular, we fix 1 lattice site $\approx 1\,\mu$m and 1 MCS ≈ 7 seconds: with this setting the simulated TECs move with nearly the experimental velocity of real vascular cells [62], and the overall patterning has a comparable time scale with respect to *in vitro* realizations (≈ 24 h [20]).

Initially, we randomly and isotropically distribute 120 virtual quiescent TECs over a square domain of 550 px $\times$ 550 px (550 μm $\times$ 550 μm), which mimics a 24-well plate, coated with a virtual Matrigel. The number of cells, which initially have the target dimensions given in Table I, is proportional to a typical experimental cell density [20]. All the other model parameters are listed in Tables I and II: in particular, there are no activated intracellular messengers AA and NO and no extracellular diffusing VEGF. Moreover, the initial calcium level is homogeneous both inside the cells, C_0, and in the external medium, $C_{ext,0}$. As shown in Fig. 4, the kinetics and the temporal dynamics of our *in silico* morphogenesis, as well as the final pattern configuration, clearly resemble experimental cultures (see also [20]). In particular, the tumor-derived endothelial cells organize into a structured network similar to a capillary plexus, where cords of cells enclose lacunae. Vascular branches typically are one or two cells wide, while lacunae reach a roughly uniform size over time, after that the smaller ones shrink and disappear. It is useful to underline that the pattern emerges autonomously, without prescribed phenomenological rules, as its formation is realistically driven by the complex and coordinated interplay of multilevel mechanisms: the calcium-dependent increase in cell motility, adhesion and cytoskeletal remodeling and the VEGF-mediated chemotactic migration. In particular, the simulated TECs realistically elongate and show the tendency to maintain the direction dictated by their longer axis,
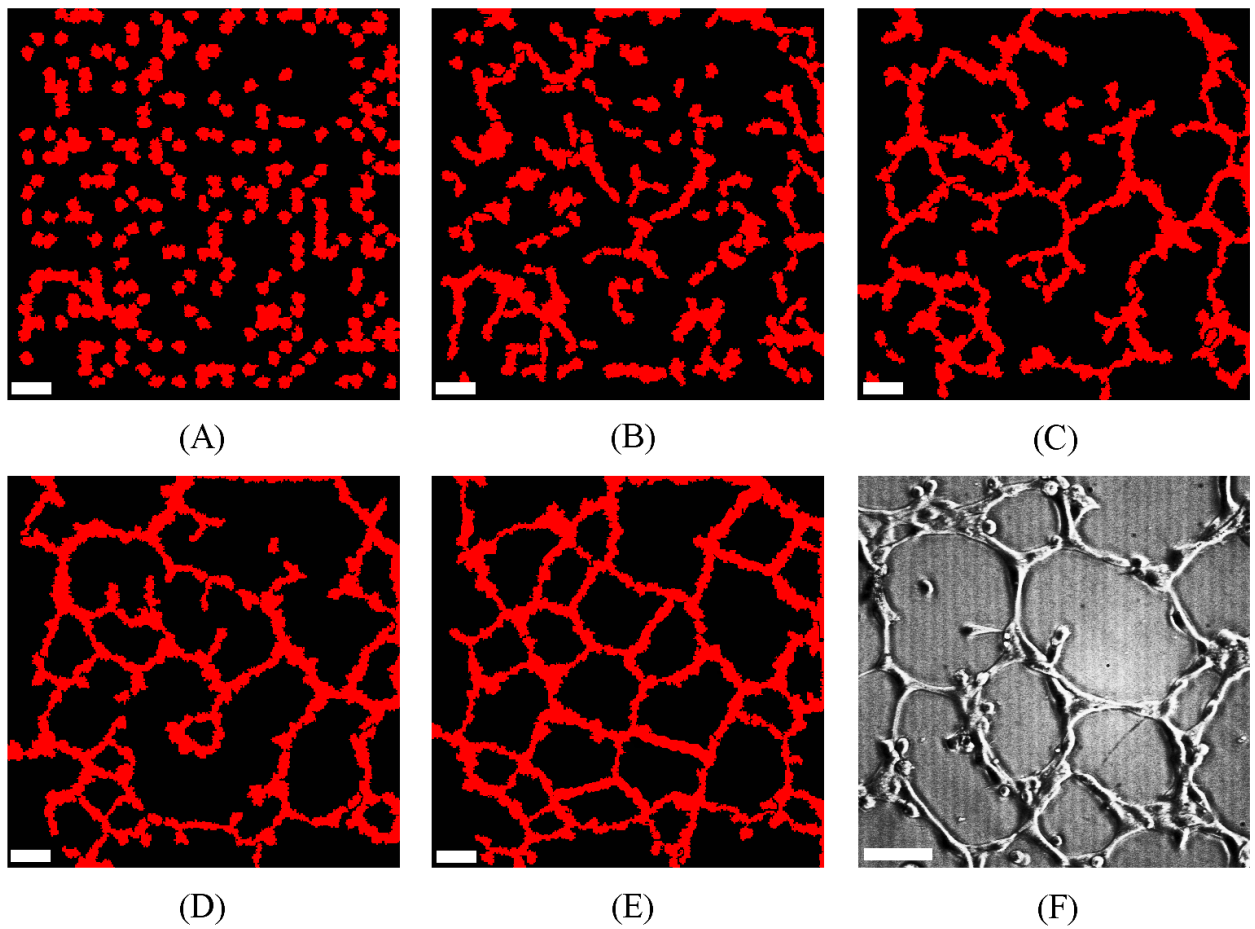
---

[2]http://www.compucell3d.org

Figure 4: Capillary-like network formation in a simulation initiated with 120 quiescent TECs over an area of 550 μm $\times$ 550 μm (550 px $\times$ 550 px). This cell density corresponds to typical *in vitro* experiments [20, 53, 68]. Representative images show different stages of tubule organization at: (A) 0, (B) 2000, (C) 4000, (D) 6000, (E) 9000, and (F) 12000 MCS. 1 MCS $\approx$ 7 seconds. All the model parameters are listed in Tables I and II. (G) reproduces the final pattern (after $\approx$ 24 h) of an experimental TEC population, courtesy of LM and of the Department of Animal and Human Biology, Universita degli Studi di Torino. White scale bars: 50 μm.

see Fig. 5. This phenomenology is fundamental for the formation of single immature capillary branches, whose following coarsening and organization are instead permitted by the cell slower sideaway fluctuations [42, 68], and has not required any *a priori* assumption on cell length (as done in similar CPMs [42]). Cell polarization is in fact the natural result of the interplay between the extracellular chemical stimulus and the intrinsic calcium-dependent cell elasticity, and it is also facilitated by the accurate compartmentalized representation of TECs.

(A)   (B)

Figure 5: Figure showing the model's ability to realistically reproduce the elongation typical of vascular cells. Magnification of samples of simulated TECs able to polarize during patterning. Representative images at (A) 0 and (B) at 1000 MCS (1 MCS $\approx$ 7 seconds). This phenomenology is a consequence of the interplay between the calcium-induced cell cytoskeletal reorganization and the VEGF chemotactic stimulus. Scale bar: 50 μm ($\approx$ 50 lattice sites).
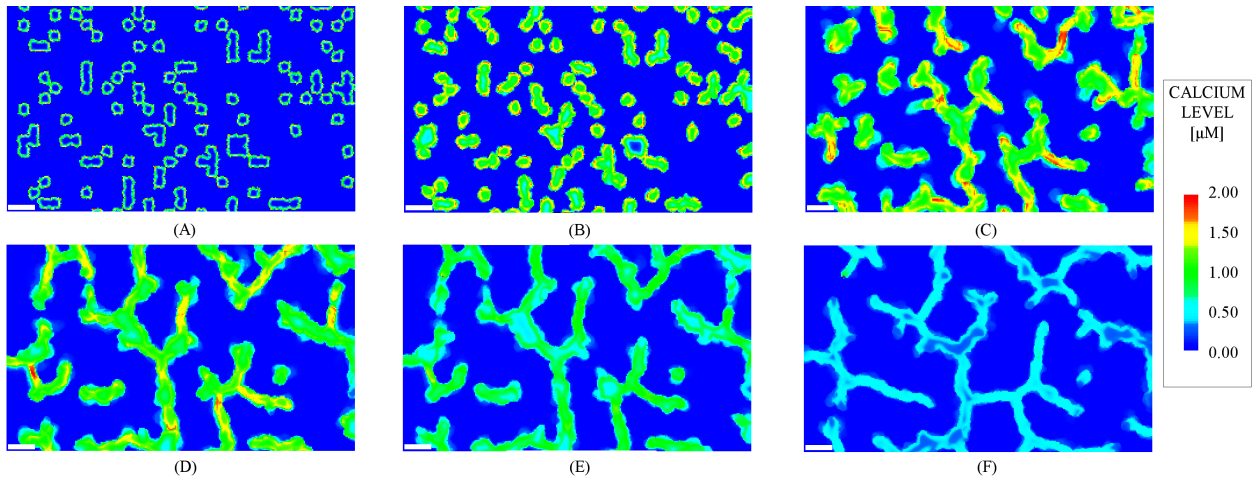

Figure 6: VEGF-induced calcium signals are down-regulated during TEC capillary-like organization. Representative images showing different stages of tubulogenic process. (A) 0, (B) 2000, (C) 4000, (D) 6000, (E) 9000, and (F) 12000 MCS (1 MCS $\approx$ 7 seconds). Scale bar: 50 μm ($\approx$ 50 lattice sites).

The model permits also a quantitative analysis of intracellular calcium events during the entire capillary-like formation. In particular, our simulations suggest that VEGF evokes calcium signals in the early phases of tubulogenesis, when TECs are not well connected in a mature network, Fig. 6A-C. Indeed, the mitogen-induced calcium events are dramatically and significantly reduced in TECs organized in more structured tubules, although they are still detectable, see Fig. 6D-F. These results are in a remarkable agreement with those reported in the literature for TEC cultures stimulated by AA [20]. The specific role of calcium signals in the first stages of vascular progression is likely to be associated with differential membrane channel functionality regulated either at the gene or at the protein level [53].

Having demonstrated the model consistency with experimental observations, we are now in the position to predict the effect of potential anti-angiogenic therapies. As a quantitative measure characterizing the final pattern (i.e., at 12000 MCS $\approx$ 24 h), we introduce the total rate of tubule length (in μm): it is defined as the sum of the lengths of all

mature cords, i.e. the structures formed by a minimum of three detectable cells and connected through a node with a similar one. In the standard parameter setting it is labeled as L_T and, on average, is $2.423 \times 10^3 \pm 5 \times 10$ μm ($\approx$ 2.423×10^3 px, mean of 20 simulations $\pm$ standard deviation), agreeing well with the measurements reported in the literature for similar cell densities [20, 53, 68]. L_T is used as the reference value: the effect of the simulated therapies (whose relative total tubule length values are identified with l_T) is in fact quantified by the percentage of reduction of L_T, i.e. pct= $1 - (l_T/L_T)$. Obviously, all the model parameters can theoretically be changed, but we will only detail biologically reasonable (and therefore most influential and predictive) variations.
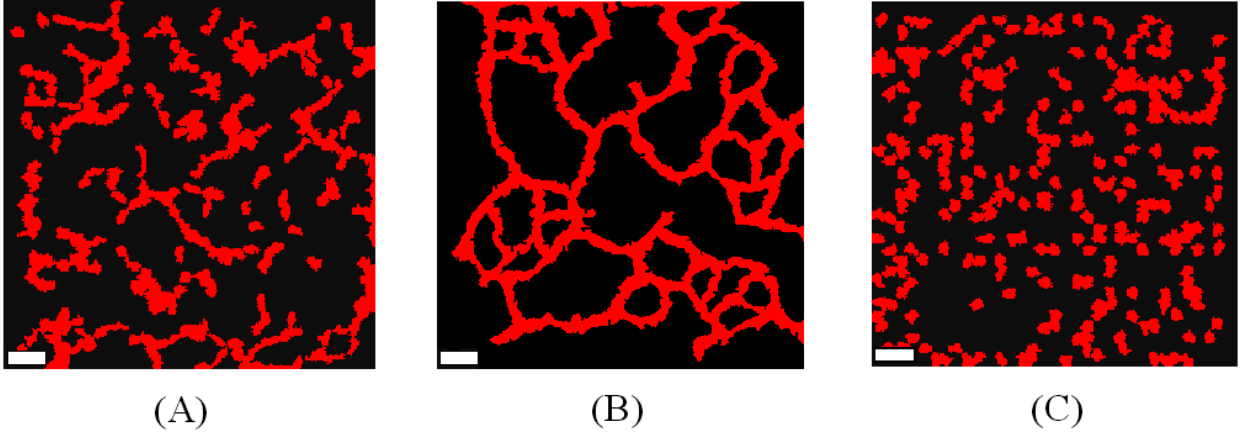

(A)   (B)   (C)

Figure 7: Increasing VEGF degradation rate (i.e., doubling λ_V in (2.14)): (A) down-regulation of network organization at $\approx$ 24 h (12000 MCS), (B) formation of a reduced-in-scale network at $\approx$ 36 h (18000 MCS). (C) disruption of patterning by inhibiting VEGF uptake by TECs (i.e., imposing $B(\mathbf{x}, t, V(\mathbf{x}, t)) = 0$ in Eq. (2.14)). All the other model parameters are the same as the basic simulation in Fig. 4. Scale bars are 50 μm long ($\approx$ 50 lattice sites).

We first test the actual clinically viable biomedical interventions. Most current drugs target the VEGF system, either by directly attacking VEGF molecules (with antibodies such as Bevacizumab and Ranimizumab or aptamers such as Pegaptanib), or by preventing the activation of its tyrosine kinase receptors (with small inhibitor molecules such as sorafenib, sunitinib, and vatalanib) [69]. We implement such interferences with VEGF activity by increasing its degradation rate (doubling λ_V in Eq. (2.14)) and, respectively, by reducing the effectiveness of its uptake (i.e., imposing $B(\mathbf{x}, t, V(\mathbf{x}, t)) = 0$ also in (2.14)). In the first case we observe a phenomenon of high interest: at the standard final time (i.e., $\approx$ 24 h) the tubulogenic process is dramatically down-regulated, confirming the effectiveness of the treatment, as $l_T \approx 0.24 \cdot L_T$ (pct=0.76), see Fig. 7A. However, at much higher times ($\gg$ 30 h) a pattern emerges, formed a number of connected networks characterized by small lacunae and short chords, see Fig. 7B. This is in somewhat agreement with theoretical results from both previous continuous [2, 24, 68] and discrete models [44]: the reduced scale of these structures is in fact dictated by the diffusion coefficient of the morphogen, which is affected by the increment of its degradation rate. However, the delay in the formation of such a reduced-in-length network is not present in those published works, and is probably due to the fact that in our model VEGF uptake has a threshold behavior (see Eq. (2.15)): a slower diffusion of the morphogen causes in fact a temporal shift in the full-activation of the calcium-dependent cascades. The overall inhibition of the activity of cell VEGF receptors results instead in a complete disruption of vascular progression, as $l_T \approx 0.08 \cdot L_T$ (pct=0.92), see Fig. 7C. Without sequestering VEGF molecules, in fact, the TECs do not completely activate the downstream intracellular cascades and therefore almost remain in resting conditions, characterized by a typical random movement.

Analogous efficient results are obtained by blocking the overall mitogen-induced calcium entry (with $F_{AA} = F_{NO} = 0$ in Eq. (2.19)): this is the model counterpart of the function of carboxyamidotriazole (CAI) compound, an anti-invasive and anti-angiogenic agent, which is able to inhibit the calcium-mediated signal transduction [20, 50]. Up to now CAI is the only calcium interfering drug successfully employed in the treatment of solid tumors (currently under investigation as an orally administered agent in phase I and II clinical trials [55]). In particular, a comparison of experimental observations and numerical results is given in Fig. 8A-B: in both cases we observe a complete disruption
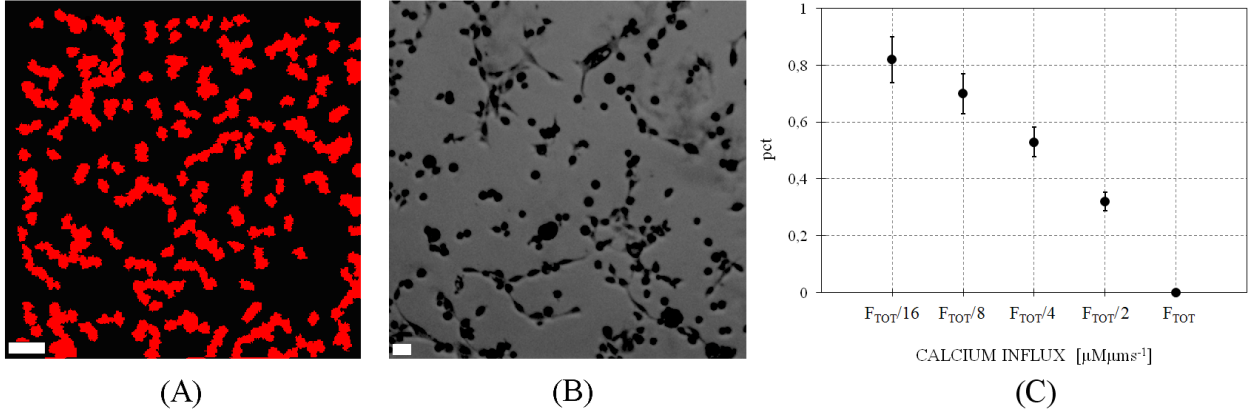
Figure 8: Complete inhibition of tubule formation in a TEC culture pretreated with saturating amounts of (A) virtual (i.e., $F_{AA} = F_{NO} = 0$ in Eq. (2.19)) and (B) experimental (i.e., 1 μM) CAI. Figure (B) courtesy of LM and of the Department of Animal and Human Biology, Universita degli Studi di Torino. Scale bars 50 μm long. (C) pct (i.e., percentage of reduction of the total tubule length) as a function of the dose of the virtual CAI, as $F_{TOT} = F_{AA} + F_{NO}$. All the other model parameters are the same as the basic simulation in Fig. 4. Error bars show standard deviation over 20 simulations.

of tubule formation, as the TECs remain almost scattered ($l_T \approx 0.12 \cdot L_T$ and, consequently, pct=0.88). This is due to the fact that a dramatic interference in mitogen-induced calcium machinery results in a clear inhibition of cell adhesive and migratory properties. Moreover, a modulated reduction of calcium influxes confirms the dose-dependent efficiency of CAI, see Fig. 8C.

By imposing $v_{AA} = c_{AA} = 0$ in Eq. (2.16) (similarly $v_{Ca-AA} = v_{NO} = 0$ in Eq. (2.17)), we simulate the exclusion of arachidonic acid (nitric oxide) biosynthesis, resembling cells pre-treated with widely used PLA2 (similarly eNOS) inhibitors (AACOCF3, similarly L-NAME or L-NMMA [46, 55]). In both cases, VEGF-mediated intracellular calcium events are not completely abolished and the relative microscopic mechanisms (i.e., enhancement of cell adhesion, motility, and chemical sensitivity) still occur, but with a significant delay and a lower intensity. Consequently, the ultimate pattern morphologies feature an immature network, where several branches have partially formed, but have not been able to organize in a single structure, see Fig. 9. In particular, the disruption of AA production leads to $l_T \approx 0.61 \cdot L_T$ (and thus pct=0.39), while the disruption of NO biosynthesis results in $l_T \approx 0.73 \cdot L_T$ (pct=0.27): this difference is caused by the fact that AA partially regulates the recruitment of NO itself, see Eq. (2.17).

A potentially more efficient intervention strategy consists in blocking the calcium-dependent cytoskeletal reorganization of TECs: in the model with a high constant $\mu_p(\sigma, \eta)$ for each σ (where $\tau(\eta) = C$, see (2.5)) and, experimentally, with phalloidin-like compounds. The resulting capillary morphology, illustrated in Fig. 10A, features in fact clumped, stunted and somewhat shorter and thicker sprouts, as l_T is $\approx 0.13 \cdot L_T$ and pct=0.87. In particular, the vascular cords are 3-4 cells wide, with larger intervascular spaces. This phenomenology is consistent with typical vascular hyperplasia [6] and is caused by the fact that TECs are forced to keep their initial round morphology and, consequently, loose the capacity to differentiate and polarize. Consequently, the TECs do not have the persistent migration needed for the formation of a functional network, as they can only form small, disconnected, branches along the gradients of VEGF concentrations (see [31] for detailed comments). Analogous results are observed with the direct exclusion of the cell directional persistence ($\mu_{pers} = 0$ in (2.11) for all cells), which is counter-intuitive and currently hard to experimentally handle. The formed sprouts are again immature and swollen, with $l_T \approx 0.27 \cdot L_T$ and pct=0.73, as depicted in Fig. 10B. Another strategy of high interest is the disruption of the chemotactic strength (by setting $\mu_{ch} = 0$ in 2.8). It causes cells to lose their directional guidance cues (they maintain a degree of directional persistence, due to the term (2.11), but are not influenced by chemical gradients) and to organize in poorly formed "vascular island" ($l_T \approx 0.14 \cdot L_T$ and pct=0.86), see Fig. 10C. This result shows that a stimulation of cell adhesion and motility, without a chemotactic mechanism, does not suffice for the maturation of a capillary-like structure, as also demonstrated experimentally by extinguish morphogen gradients in [68], and theoretically in other Potts models [42, 43]. A further
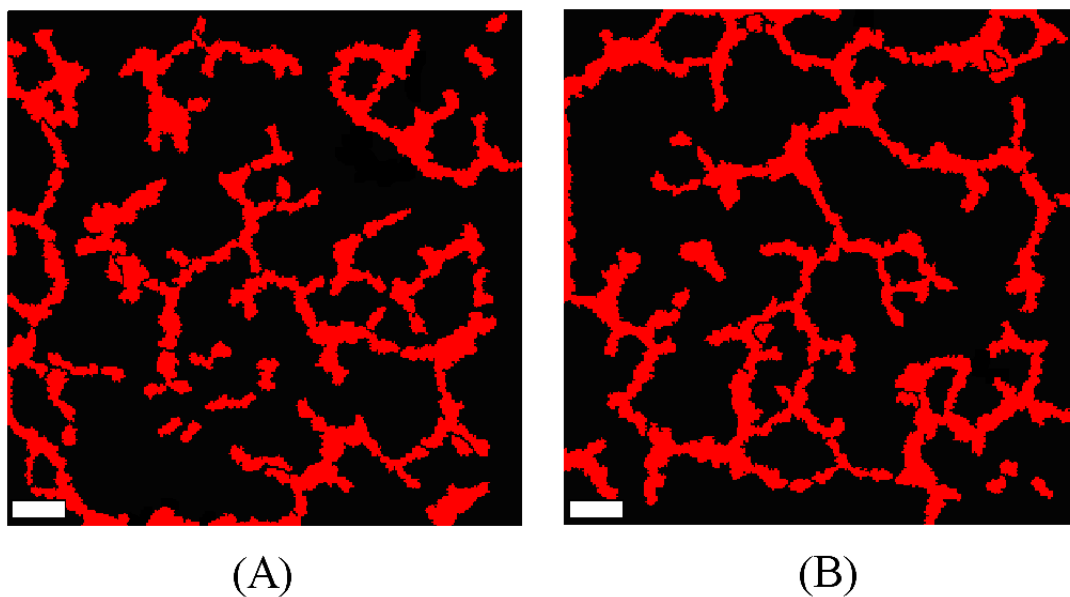
14

Figure 9: Partial disruption of TEC tubule formation by inhibiting (A) AA production (by imposing $v_{AA} = c_{AA} = 0$ in Eq. (2.16), which is the model counterpart of the activity of AACOCF3 compound) and (B) NO biosynthesis (by imposing $v_{Ca-AA} = v_{NO} = 0$ in Eq. (2.17), which is the model counterpart of the activity of L-NAME or L-NMMA compounds). All the other model parameters are the same as the basic simulation in Fig. 4. Scale bars are 50 μm long ($\approx$ 50 lattice sites).
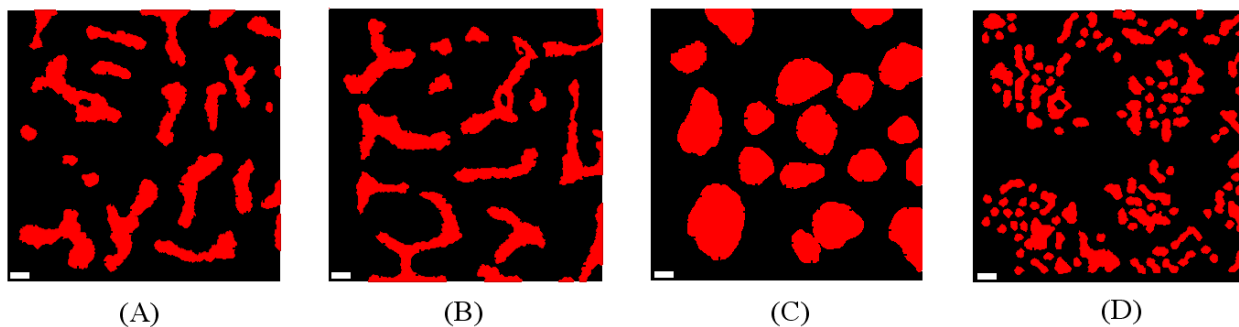

Figure 10: Example morphologies from proposed anti-angiogenic therapies. A quantitative review is given in Figure 4. Disruption of (A) cytoskeletal reorganization, (B) persistence, (C) chemotaxis, and (D) adhesion. For each case, all the other model parameters are the same as the basic simulation in Fig. 4. Scale bars are 50 μm long ($\approx$ 50 lattice sites).

trivial, but possible, anti-angiogenic strategy deals with the interference in the cell adhesive strengths. In particular, a high spatially homogeneous value of $J^{ext}(C, C)$ is the computational counterpart of the function of anti-VE-cadherin antibodies, which block VE-cadherin receptors preventing the formation of contact junctions between cells. This intervention produces aggregates of dispersed TECs, which are located in the zones of higher VEGF concentrations ($l_T \approx 0.06 \cdot L_T$, pct=0.94), as reproduced in Fig. 10D.

Reviewing our results, in Fig. 11, it is satisfying to see that the model has realistically reproduced the effects of some anti-angiogenic strategies actually in use and has been able to propose unexpected but potentially efficient therapies, which require further investigations, eventually *in vitro*. In particular, the percentage of reduction of the total tubule length (i.e., pct) has been compared in the different cases using a one-sided equal-variance t-test with a Bonferroni correction as a scoring method [61]. The level of significance has been taken P < 0.005.

4   Discussion

Tumor angiogenesis is an important step in cancer development, based on an intricate interaction between multiple levels of organization: the molecular, the cellular and the tissue scales. The ability of tumor-derived endothelial cells to organize in a functional capillary plexus is in fact largely mediated by a series of cellular and molecular mechanisms, regulated by external signals, such as VEGF stimulation, together with cell-cell interactions. However, the driving components of malignant vascularization are still not fully biologically clarified. The constant challenge of understanding these mechanisms and, eventually, to propose biomedical therapies able to disrupt them has thus lead to many continuous [2, 24, 68] and discrete [41, 42, 43] mathematical models.

In particular, previous cell-based models have focused on the effect of a diffusible VEGF and, although without incorporating the underpinning intracellular biochemical and biophysical dynamics, have provided important new insights and complete descriptions of the morphology and phenomenology of nascent capillary-like patterns. Our work has used these approaches as a useful starting point for the construction of an innovative multilevel and hybrid model that is characterized by a realistic representation of cells and by an accurate derivation of their biophysical properties, described by standard CPM parameters, from microscopic subcellular mechanisms and relative signalling pathways. In particular, starting from some other published CPM applications, that use a compartmentalization approach for biological cells, also included as a standard feature of the CompuCell3D package [25, 40, 79], we have made a further step forward introducing a set of compartments characterized by their immediate and direct correspondence to real subcellular elements. Indeed, this is the first time that, in a CPM, the cells are accurately differentiated between the nucleus and the cytosolic region (see [67] form more details). Furthermore, our model has been able to derive the cells' biophysical properties, behaviors and phenomenology from biologically consistent VEGF-induced calcium-dependent subcellular mechanisms, without prescribing a set of *a priori* rules, which are often used in similar approaches. Finally, whenever possible, we have used parameters taken from experiments directly made on tumor-derived endothelial cells, as reposted in the included references.

Our cell-based approach has been able to capture and reproduce basic and fundamental mechanisms of *in vitro* tubule progression, such as cell elongation, adhesion and preferential migration along chemotactic cues, as well as more complex events, such as intracellular calcium signaling. Moreover, the model has permitted to identify and to virtually test specific and biologically reasonable investigations of potential anti-angiogenic strategies. In particular, reviewing the results, this computational method has confirmed the efficiency of current therapies (focusing on the interferences with VEGF activity or with calcium machinery), and has quickly suggested novel and interesting cancer therapies. All the proposed solutions have in fact the potential to dramatically reduce the angiogenic phenotype of tumor-derived endothelial cells in unexpected multiple ways and have emerged by opportune and biologically reasonable variations in model parameters. In particular, we have made some predictions about the possible success of therapies blocking the mechanisms of either cytoskeletal remodeling or increase in cellular adhesion. The development of interventions inhibiting cell chemotaxis and persistent movement may be also optimal strategies. Even though it is possible to form a *post hoc* explanation of each solution's effectiveness, it is unlikely that these solutions would have been manually discovered. However, the transition from *in silico* to *in vitro* and, in turn, to *in vivo* investigations

16

OPTIMAL POTENTIAL THERAPIES
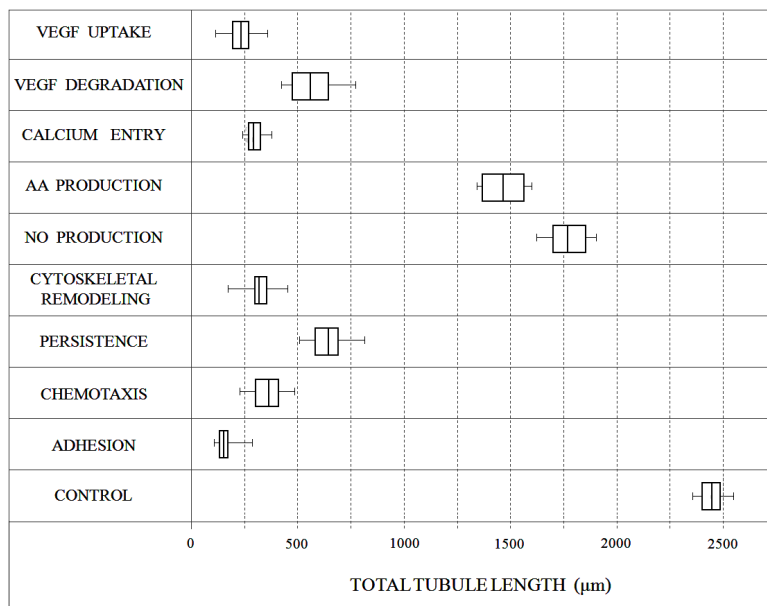
	MODEL PARAMETER	EXISTING COMPOUND	P-VALUE (pct)	EFFICIENCY
VEGF UPTAKE	β_V	sorafenib, sunitinib, vatalanib	0.00082	+++
VEGF DEGRADATION	λ_V		0.00234	++
CALCIUM ENTRY	F_{AA}, F_{NO}	CAI	0.00085	+++
AA PRODUCTION	v_{AA}, c_{AA}	AACOCF3	0.00425	+
NO PRODUCTION	$v_{Ca\text{-}AA}$, v_{NO}	L-NAME, L-NMMA	0.00473	+
CYTOSKELETAL REMODELING	μ_{pers}	phalloidin	0.00092	+++
PERSISTENCE	μ_{in}		0.00139	++
CHEMOTAXIS	μ_{ch}		0.00097	+++
ADHESION	J^{ext} (C,C)	anti-VE-cadherin antibodies	0.00069	+++

Figure 11: Optimal potential anti-angiogenic therapies found by model disruptions (control solution represents the no treatment case, with no changes in the parameter, and corresponds to simulation of Fig. 4). Top panel: box plot of the total tubule length (in μm), with 20 simulations for each simulated strategy. Bottom panel: table of the proposed therapies with their relative modified parameters and, whenever currently available, the existing experimental drugs. Forth column of the table gives a statitistical test for each intervention: the percentage of reduction of the total tubule length (pct) has has been evaluated with a one-sided equal-variance t-test with a Bonferroni correction, which tests the hypothesis $\overline{pct} > 0$ against the alternative $\overline{pct} = 0$, where $\overline{pct}$ is the mean over 20 simulations of pct, with a level of significance P < 0.005 [61]. In particular, for P < 0.001 we have an optimal solution (labeled with +++ in the table), for 0.001 < P < 0.003 we have a suboptimal solution, ++, while for 0.003 < P < 0.005 we have a bad solution, +.

implies obvious complications due to the recruitment of cell types other than endothelial cells involved in tumor vascularization and to potential unexpected side effects.

Our model can be refined by providing a finer degree of the used VEGF-induced cascade as well as by including other regulatory pathways. Further structural and functional information on calcium channels will also help finding out more specific ways to interfere with tubule formation. In particular, we cannot exclude the existence of channels co-modulated by AA and NO and of potential cross regulations between different channel types: for example, several members of the TRP family (in particular TRPC and TRPV sub-families) can be involved in the angiogenic progression [36, 53, 54, 56]. Another possible development of the model is the inclusion of active ECM-like substrates, which can also be differentiated for their mechanical properties, such as concentration, stiffness and elasticity. In the present version of our approach we in fact neglect cell-matrix interactions and mechanisms of matrix remodeling, like secretion of protein or degrading enzymes by TECs: however, they are likely important in tubule formation, especially in three dimensions. A further plausible hypothesis is that ECM is also able to trap VEGF molecules generating shorter, steeper gradients around the cells: the consequent decrease in morphogen diffusion can ultimately affect tubule formation. Moreover, relations (2.9) and (2.10) are a model simplifications: new microfluidics quantitative analysis have in fact suggested that the interdependencies between the gradients of the VEGF, its concentration and the chemotactic response would be more complicate. In particular, a minimum number of VEGF molecules seems to be necessary for a chemotactic response, as long as minimum steepness of the VEGF gradients [17]. Finally, we hope to add another scale to the system by mechanistically linking the quantitative expression of intracellular messengers to a gene network dynamics. This further level of investigation will be an important consideration for in-depth analysis of the controlling mechanisms of tumor angiogenesis and could be used as a new point of view for future therapeutic searches.

References

[1] Albrecht, M. A., Colegrove, S., L., Friel, D. D., 2002. *Differential regulation of ER Ca2+ uptake and release rates accounts for multiple modes of Ca2+-induced Ca2+ release.* J Gen Physiol, 119 (3), 211 - 233.

[2] Ambrosi, D., Gamba, A., Serini, G., 2004. *Cell directional persistence and chemotaxis in vascular morphogenesis* Bull Math Biol, 66 (6), 1851 - 1873.

[3] Ambrosi, D., Bussolino F., Preziosi, L., 2005. *A review of vasculogenesis models.* J Theor Med, 6, 1 - 19.

[4] Baluk, P., Morikawa, S., Haskell, A., Mancuso, M., McDonald, D. M., 2003. *Abnormalities of basement membrane on blood vessels and endothelial sprouts in tumors.* Am J Pathol, 163, 1801 - 1815.

[5] Bayley, P., Ahlstrom, P., Martin, S. R., Forsen S., 1984. *The kinetics of calcium binding to calmodulin: Quin 2 and ANS stopped-flow fluorescence studies.* Biochem Biophys Res Commun, 120 (1), 185 – 191.

[6] Bauer, A. L., Jackson, T. L., Jiangy, Y., 2007. *A cell-based model exhibiting branching and anastomosis during tumor-induced angiogenesis* Biophys J, 92, 3105 - 3121.

[7] Berridge, M. J., Bootman, M. D., Roderick, H. L., 2003. *Calcium signalling: dynamics, homeostasis and remodelling.* Nat Rev Mol Cell Biol, 4 (7), 517 - 529.

[8] Berridge, M. J., 1995. *Calcium signalling and cell proliferation.* Bio Essays, 17, 491 - 500.

[9] Berridge, M. J., Lipp, P., Bootman, M. D., 2000. *The versatility and universality of calcium signalling.* Nature Rev, 1, 11 - 21.

[10] Boonstra, J., Van Rossum, G. S., 2003. *The role of cytosolic phospholipase A2 in cell cycle progression.* Prog Cell Cycle Res, 5, 181 - 190.

[11] Bootman, M. D., Lipp, P., Berridge, M. J., 2001. *The organisation and functions of local Ca2+ signals.* J Cell Sci, 114 (12), 2213 - 2222.

[12] Bussolati, B., Deregibus, M. C., Camussi, G., 2010. *Characterization of molecular and functional alterations of tumor endothelial cells to design anti-angiogenic strategies.* Curr Vasc Pharmacology, In Press.

[13] Bussolino, F., Arese, M., Audero, E., Giraudo, E., Marchio, S., Mitola, S., Primo, L., Serino, G., 2003. *Biological aspects in tumor angiogenesis.* In Preziosi, L. editor, *Cancer modeling and simulation*, Mathematical Biology and Medicine Sciences, Chapman and Hall/CRC, 1 - 16.

[14] Carmeliet, P., Jain, R. K., 2000. *Angiogenesis in cancer and other diseases.* Nature, 407, 249 - 257.

[15] Carmeliet, P., 2005. *Angiogenesis in life, disease and medicine.* Nature, 438, 932 - 936.

[16] Carmeliet, P., 2005. *VEGF as a key mediator of angiogenesis in cancer.* Oncology, 69, 4 - 10.

[17] Chen, R. R., Silva, E. A., Yuen, W. W., Brock, A. A., Fischbach, C., Lin, A. S., Guldberg, R. E., Mooney, D. J., 2007. *Integrated approach to designing growth factor delivery system.* FASEB J, 21 (14), 3896 - 3903

[18] Coatesworth, W., Bolsover, S., 2008. *Calcium signal transmission in chick sensory neurones is diffusion based.* Cell Calcium, 43 (3), 236 - 49.

[19] Fink, C. C., Slepchenko, B., Moraru, I. I., Watras, J., Schaff, J. C., Loew, L. M., 2000. *An image-based model of calcium waves in differentiated neuroblastoma cells.* Biophys J, 79 (1), 163 - 183.

[20] Fiorio Pla, A., Grange, C., Antoniotti, S., Tomatis, C., Merlino, A., Bussolati, B., Munaron, L., 2008. *Arachidonic acid-induced Ca2+ entry is involved in early steps of tumor angiogenesis.* Mol Cancer Res, 6 (4), 535 - 545.

[21] Fiorio Pla, A., Munaron, L., 2001. *Calcium influx, arachidonic acid, and control of endothelial cell proliferation.* Cell Calcium, 30 (4), 235 - 244.

[22] Fiorio Pla, A., Genova, T., Pupo, E., Tomatis, C., Genazzani, A., Zaninetti, R., Munaron, L., 2010. *Multiple roles of protein kinase a on arachidonic acidmediated Ca2+ entry and tumor-derived human endothelial cells migration.* Mol Cancer Res, In press.

[23] Fleming, I., and Busse, R., 1999. *Signal transduction of eNOS activation.* Cardiovasc Res, 43, 532 - 541.

[24] Gamba, A., Ambrosi, D., Coniglio, A., de Candia, A., di Talia, S., Giraudo, E., Serini, G., Preziosi, L., Bussolino, F., 2003. *Percolation, morphogenesis, and Burgers dynamics in blood vessel formation.* Phys Rev Letters, 90 (11), 101 - 118.

[25] Glazier, J. A., Balter, A., Merks, R. M. H., Poplawski, N. J., Swat, M., 2007. *The Glazier-Graner-Hogeweg model: extension, future direction, and opportunitites for further study.* Single-Cell-Based Model Biol Med, 4, 157 - 167 (Chapter II).

[26] Glazier, J. A., Balter, A., Poplawski, N. J., 2007. *Magnetization to morphogenesis: a brief history of the Glazier-graner-Hogeweg model.* In A. R. A. Anderson, M. A. J. Chaplain, and K. A. Rejniak editors, *Single-Cell-Based Models in Biology and Medicine*, Mathematics and Biosciences in Interactions, Birkaüser, 79 - 106.

[27] Glazier, J. A., Graner, F., 1993. *Simulation of the differential adhesion driven rearrangement of biological cells.* Phys Rev E, 47, 2128 - 2154.

[28] Goto, Y., Miura, M., Iijima, T., 1996. *Extrusion mechanisms of intracellular Ca2+ in human aortic endothelial cells.* Eur J Pharmacol, 314 (1-2), 185 - 192.

[29] Graner, F., Glazier, J. A., 1992. *Simulation of biological cell sorting using a two dimensional extended Potts model.* Phys Rev Lett, 69, 2013 - 2017.

[30] Hryshko, L., V., Philipson, K., D., 1997. *Sodium-calcium exchange: recent advances.* Basic Res Cardiol, 92 (1), 45 - 51.

[31] Huang, S., Brangwynne, C. P., Parker, K. K., Ingber, D. E., 2005. *Symmetry-breaking in mammalian cell cohort migration during tissue pattern formation: role of random-walk persistence.* Cell Motil Cytoskeleton, 61, 201 - 213.

[32] Jain, R. K., 2003. *Molecular regulation of vessel maturation.* Nat Med, 9, 685 - 693.

[33] Khanapure, S. P., Garvey, D. S., Janero, D. R., Letts, L., G., 2007. *Eicosanoids in inflammation: biosynthesis, pharmacology, and therapeutic frontiers.* Curr Top Med Chem, 7 (3), 311 - 340.

[34] Kimura, H., Esumi, H., 2003. *Reciprocal regulation between nitric oxide and vascular endothelial growth factor in angiogenesis.* Acta Biochim Pol, 50 (1), 49 - 59.

[35] Klingauf, J., Neher, E., 1997. *Modeling buffered Ca^{2+} diffusion near the membrane: implications for secretion in neuroendocrine cells.* Biophys J, 72, 674 - 690.

[36] Kwan, H. Y., Huang, Y., Yao, X., 2007. *TRP channels in endothelial function and dysfunction.* Biochim Biophys Acta, 1772, 907 - 914.

[37] Lahat, N., Sheinfeld, M., Sobel, E., Kinarty, A., Kraiem, Z., 1992. *Divergent effects of cytokines on human leukocyte antigen-DR antigen expression of neoplastic and non- neoplastic human thyroid cells.* Cancer Surv, 69, 1799 - 1807.

[38] Leith, J. T., Michelson, S., 1995. *Secretion rates and levels of vascular endothelial growth factor in clone-a or Hct-8 human colon tumor cells as a function of oxygen concentration.* Cell Prolif, 28, 415 - 430.

[39] Marée, A. F. M., Grieneisen, V. A., Hogeweg, P., 2007. *The Cellular Potts Model and biophysical properties of cells, tissues and morphogenesis.* In A. R. A. Anderson, M. A. J. Chaplain, and K. A. Rejniak editors, *Single-Cell-Based Models in Biology and Medicine*, Mathematics and Biosciences in Interactions, Birkaüser, 107 - 136.

[40] Marée, A. F. M., Jilkine, A., Dawes, A., Grieneisen, V. A., Edelstein-Keshet, L., 2006. *Polarization and movement of keratocytes: A multiscale modelling approach.* B Math Biol, 68 (5), 1169 – 1211.

[41] Merks, R. M. H., Glazier, J. A., 2006. *Dynamic mechanisms of blood vessel growth.* Inst Phys Publ, 19, C1 - C10.

[42] Merks, R. M. H., Glazier, J. A., Brodsky, S. V., Goligorksy, M. S., Newman, S. A., 2006. *Cell elongation is key to in silico replication of in vitro vasculogenesis and subsequent remodeling.* Develop Biol, 289, 44 - 54.

[43] Merks, R. M. H., Perryn, E. D., Shirinifard, A., Glazier, J. A., 2008. *Contact-inhibited chemotactic motility: role in de novo and sprouting blood vessel growth.* PLOS Comp Biol, 4, e1000163.

[44] Merks, R. M. H., Newman, S. A., Glazier, J. A., 2004. *Cell-oriented modeling of in vitro capillary development.* In: Sloot PMA, Chopard B, Hoekstra AG, eds. Cellular Automata: 6th International Conference on Cellular Automata for Research and Industry. Berlin: Springer Verlag, Lect Notes Comput Sc, 3305, 425 - 434.

[45] Metropolis, N., Rosenbluth, A. E., Rosenbluth, M. N., Teller, A. H., Teller, E., 1953. *Equation of state calculations by fast computing machines.* J Chem Phys, 21, 1087 - 1092.

[46] Mottola, A., Antoniotti, S., Lovisolo, D., Munaron, L., 2005. *Regulation of noncapacitative calcium entry by arachidonic acid and nitric oxide in endothelial cells.* FASEB J, 19 (14), 2075 - 2077.

[47] Munaron, L., 2002. *Calcium signalling and control of cell proliferation by tyrosine kinase receptors (review).* Int J Mol Med, 10 (6), 671 - 676.

[48] Munaron, L., 2006. *Intracellular calcium, endothelial cells and angiogenesis.* Recent Patents Anticancer Drug Discov, 1 (1), 105 - 119.

[49] Munaron, L., Antoniotti, S., Distasi, C., Lovisolo, D., 1997. *Arachidonic acid mediates calcium influx induced by basic fibroblast growth factor in Balb-c 3T3 fibroblasts.* Cell Calcium, 22 (3), 179 - 188.

[50] Munaron, L., Antoniotti, S., Fiorio Pla, A., Lovisolo, D., 2004a. *Blocking Ca2+entry: a way to control cell proliferation.* Curr Med Chem, 11 (12), 1533 - 1543.

[51] Munaron, L., Antoniotti, S., Lovisolo, D., 2004b. *Intracellular calcium signals and control of cell proliferation: how many mechanisms?* J Cell Mol Med, 8 (2), 161 - 168.

[52] Munaron, L., Fiorio Pla, A., 2000. *Calcium influx induced by activation of tyrosine kinase receptors in cultured bovine aortic endothelial cells.* J Cell Physiol, 185 (3), 454 - 463.

[53] Munaron, L., Tomatis, C., Fiorio Pla, A., 2008. *The secret marriage between calcium and tumor angiogenesis.* Technol Cancer Res Treat, 7 (4), 335 - 339.

[54] Munaron, L., 2009. *A tridimensional model of proangiogenic calcium signals in endothelial cells.* The Open Biology J, 2, 114 - 129.

[55] Munaron, L., Fiorio Pla, A., 2000. *Endothelial calcium machinery and angiogenesis: understanding physiology to interfere with pathology.* Current Medicinal Chemistry, 16, 4691 - 4703.

[56] Nilius, B., Droogmans, G., 2001. *Ion channels and their functional role in vascular endothelium.* Physiol Rev, 81, 1415 - 1459.

[57] Pacher, P., Beckman, J. S., Liaudet, L., 2007. *Nitric oxide and peroxynitrite in health and disease.* Physiol Rev, 87 (1), 315 - 424.

[58] Patton, A. M., Kassis, J., Doong, H., Kohn, E. C., 2003. *Calcium as a molecular target in angiogenesis.* Curr Pharm Des, 9, 543 - 51.

[59] Perryn, E. D., Czirok, A., Little, C. D., 2008. *Vascular sprout formation entails tissue deformations and VE-cadherin dependent cell-autonomous motility.* Dev Biol, 313, 545 - 555.

[60] Poplawski, N. J., Shirinifard, A., Swat, M., Glazier, J. A., 2008. *Simulation od single–species bacterical–biofilm growth using the Glazier–Graner–Hogeweg model and the CompuCell3D modeling environment.* Math Biosci Eng, 5, 355 - 388.

[61] Ross S.M., 2003. *Probabilitá e statistica per l'ingegneria e le scienze.* Apogeo.

[62] Rupp, P. A., Czirk, A., Little, C. D., 2004. *$\alpha v \beta 3$ integrin-dependent endothelial cell dynamics in vivo.* Development, 131, 2887 - 2897.

[63] Santella, L., Ercolano, E., Nusco, G. A., 2005. *The cell cycle: a new entry in the field of Ca2+ signaling.* Cell Mol Life Sci, 62 (21), 2405 - 2413

[64] Savill, N. J., Hogeweg, P., 1997. *Modelling morphogenesis: from single cells to crawling slugs.* J Theor Biol, 184, 118 – 124.

[65] Scianna, M., Merks, R. M. H., Preziosi, L., Medico, E., 2009. *Individual cell-based models of cell scatter of ARO and MLP-29 cells in response to hepatocyte growth factor.* J Theor Biol, 260, 151 - 160.

[66] Scianna, M., Munaron, L., Preziosi, L., 2010. *A multiscale individual cell-based model for pro-angiogenic calcium signals in endothelial cells.* Submitted.

[67] Scianna, M., Preziosi, L., 2010. *Multiscale Developments of the Cellular Potts Model.* Submitted.

[68] Serini, G., Ambrosi, D., Giraudo, E., Gamba, A., Preziosi, L., Bussolino, F., 2003. *Modeling the early stages of vascular network assembly.* EMBO J, 22, 1771 - 1779.

[69] Shojaei, F., Ferrara, N., 2007. *Antiangiogenic therapy for cancer: an update.* The cancer J, 13 (6), 345 - 348.

[70] Sneyd, J., Keizer, J., Sanderson, M. J., 1995. *Mechanisms of calcium oscillations and waves: a quantitative analysis.* FASEB J, 9, 1463 - 1472.

[71] Sneyd, J., Keizer, J., 2009. *Mathematical Physiology.* In Interdisciplinary Applied Mathematics, Springer, USA.

[72] Steinberg, M. S., 1963. *Reconstruction of tissues by dissociated cells. Some morphogenetic tissue movements and the sorting out of embryonic cells may have a common explanation.* Science, 141, 401 – 408.

[73] Steinberg, M. S., 1970. *Does differential adhesion govern self-assembly processes in histogenesis? Equilibrium configurations and the emergence of a hierarchy among populations of embryonic cells.* J Exp Zool, 173 (4), 395 – 433.

[74] Straume, O., Salvesen, H. B., Akslen, L. A., 1999. *Angiogenesis is prognostically important in vertical growth phase melanomas.* Int J Oncol, 15, 595 - 599.

[75] Tomatis, C., Fiorio Pla, A., Munaron, L., 2007. *Cytosolic calcium microdomains by arachidonic acid and nitric oxide in endothelial cells.* Cell Calcium, 41 (3), 261 - 269.

[76] Tosin, A., Ambrosi, D., Preziosi, L., 2006. *Mechanics and chemotaxis in the morphogenesis of vascular networks.* Bull Math Biol, 68, 1819 - 1836.

[77] Valant, P. A., Adjei, P. N., Haynes, D. H., 1992. *Rapid Ca2+ extrusion via the Na+/Ca2+ exchanger of the human platelet.* J Membr Biol, 130 (1), 63 - 82.

[78] Watson, E. L., Jacobson, K. L., Singh, J. C., Di Julio, D. H., 2004. *Arachidonic acid regulates two Ca2+ entry pathways via nitric oxide.* Cell Signal, 16, 157 - 165.

[79] Walther, T., Reinsch, H., Grosse, A., Ostermann, K., Deutsch, A., Bley, T., 2004. *Mathematical modeling of regulatory mechanisms in yeast colony development.* J Theor Biol, 229, 327 – 338.